Controlling nonlinear rogue-wave formation using the coherence length of phase noise

Saumya Choudhary [1,*] A. Nicholas Black [2] Aku Antikainen [1] and Robert W. Boyd [1,2,3]

[1]*Institute of Optics, University of Rochester, Rochester, New York 14627, USA*

[2]*Department of Physics and Astronomy, University of Rochester, Rochester, New York 14627, USA*

[3]*Department of Physics, University of Ottawa, Ottawa, Ontario, K1N 6N5, Canada*

(Received 11 October 2022; accepted 19 January 2024; published 16 February 2024)

Weak phase noise present on an optical field can be amplified by a self-focusing nonlinearity ($n_2 > 0$) and form intense "rogue-wave" features. Here, we study the effect of the coherence length (or grain size) of this phase noise on the likelihood of rogue-wave formation in the presence of a self-focusing nonlinearity. We show that while the likelihood of rogue-wave formation increases with laser power when the coherence length is only slightly smaller than the beam diameter, the likelihood is minimally affected by a change in laser power when the coherence length is significantly smaller than the beam diameter. Our study provides insight into the interaction of nonlinearity with phase instabilities on a field and could be useful in applications such as reducing the effect of turbulence-induced breakup of intense laser beams, and developing radiance limiters to reduce the focusable power in a beam.

DOI: 10.1103/PhysRevResearch.6.013174

I. INTRODUCTION

The formation of rare but extreme (or "rogue") amplitude waves in optical [1–6], microwave [7], and hydrodynamic systems [8] have attracted considerable recent interest [9–11]. A random phase fluctuation with sufficient strength imposed on an optical field can develop on propagation into networklike intensity patterns that are commonly referred to as "caustics" [3,6,12]. Light can concentrate very tightly in caustics, which facilitates rogue-wave formation and leads to long-tailed statistics for the intensity and non-Rayleigh statistics for the amplitude. Rogue waves in linear systems can develop through the constructive interference of several waves with random phases and amplitudes [13], or through the directional focusing of these waves [14]. Speckle formation in optical systems is also a linear phenomenon, and the complex amplitude of a fully developed speckle field has circular Gaussian statistics with a negative exponential distribution of intensity [15,16]. Long-tailed intensity statistics in linear systems can occur due to multiple scattering through a medium [17], due to the spatial inhomogeneity-induced clustering of speckles with different grain sizes [18], and through the redistribution of energy among several speckle grains in the farfield due to higher-order correlations encoded onto the field [19].

The presence of nonlinearity in an optical system can considerably influence the formation of rogue waves. Rogue events have been observed during supercontinuum generation in nonlinear fiber-optics systems and are the result of collisions between "breather" solitons formed by nonlinear amplification of modulational instability in the system [1,10,20,21]. Rogue waves can also form in spatially extended nonlinear systems either by means of self-focusing seeded by wavefront perturbations on the field [4,6,22] or by hypercycle amplification after the breaking of spatial symmetry in optical cavities [23]. Small scale filamentation is another phenomenon that occurs when a large self-focusing nonlinearity amplifies angular spectral sidebands through four-wave mixing, leading to the formation of several localized structures called "filaments" such that each filament has the same (critical) power P_{cr} [24,25]. Rogue waves can also form in a beam undergoing small-scale filamentation when filaments merge because of medium inhomogeneities [25]. A self-focusing nonlinearity can enhance rogue-wave formation in laser beams containing weak phase noise [6]. However, a nonuniform polarization structure on the beam can suppress rogue waves under certain conditions [26]. Rogue waves are more likely to form in speckle patterns of a particular coherence length propagating through a photorefractive crystal due to the saturation of nonlinearity once a rogue feature reaches a certain minimum width [5]. Light scattered through a medium with tailored disorder can also show a similar enhancement of rogue-wave formation at a particular coherence length of the disorder [27].

Here, we study how the transverse spatial coherence length of phase noise affects rogue-wave formation in the presence of a self-focusing nonlinearity. We measure the intensity statistics of the beam after it propagates through a hot rubidium vapor cell for various coherence lengths (or grain sizes) of the phase noise and various beam powers. We observe that the intensity statistics have a diminished sensitivity to nonlinearity when the coherence length of the phase noise is much smaller than the beam width. We also study the mechanism behind

*schoudha@ur.rochester.edu

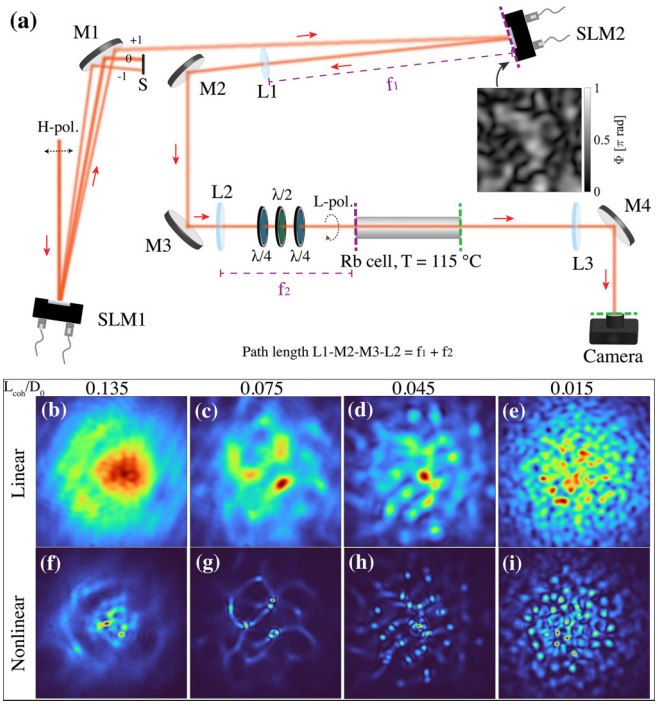

FIG. 1. (a) Schematic of the experimental setup. H-polarized light from a tunable diode laser is diffracted by a phase-only grating on spatial light modulator SLM1 forming a Gaussian beam of diameter D_0 (to $1/e^2$ values of the intensity) in the first diffractive order. SLM2 adds a random phase mask (example shown in the inset) with coherence length $L_{\rm coh}$ and amplitude of π rad on the beam. The active area of SLM2 is then relayed to the entrance facet (purple dashed line) of a 7.5-cm-long rubidium cell through a telescope formed by lenses L1 (focal length $f_1 = 1$ m) and L2 (focal length $f_2 = 0.75$ m). The output facet (green dashed line) of the cell is then imaged by lens L3 onto the image plane of the camera. Measured caustic patterns formed by noisy beams with $L_{\rm coh}/D_0$ of [(b) and (f)] 0.135, [(c) and (g)] 0.075, [(d) and (h)] 0.045, and [(e) and (i)] 0.015, after linear (top), and nonlinear (bottom) propagation through the cell are also shown. The beam power at the input of the cell ($P_{\rm in}$) was 90 mW for the nonlinear results. The focal lengths of the lenses L1, L2, and L3 are 1 m, 75 cm, and 30 cm, respectively.

this effect through numerical simulations of nonlinear beam propagation. Our simulations show that small-grained phase noise induces the redistribution of beam power into multiple filaments of reduced intensity, thereby limiting the maximum intensity in a rogue feature relative to the background. Our study complements Refs. [5,6,26], and is relevant for the development of better optical power limiters, and for probing a turbulent medium and mitigating its effect on the propagation of intense laser beams.

II. EXPERIMENT

Figure 1(a) shows the schematic of our experimental setup. Our saturable nonlinear medium is a cell containing natural abundance rubidium. We heat the cell to 115 °C, and blue detune our laser source by 600 MHz above the ^{87}Rb D_2 $F = 1 \rightarrow F' = 2$ transition in order to have a self-focusing nonlinear response. A horizontally polarized beam from our laser source diffracts from a phase grating impressed on a spatial light modulator (SLM1) and forms a Gaussian beam of diameter 2.5 mm (D_0) in the first diffractive order. We isolate this diffractive order by letting the light propagate over 2 m, and add a conjugate defocus on SLM1 to compensate for the accumulated defocus on the beam. Both SLM1 and SLM2 are liquid-crystal-on-silicon (LCOS) phase only SLMs from Hamamatsu that have identical resolution (600 × 800) and pixel size (20 μm). SLM2 adds a random phase mask with a spatial coherence length $L_{\rm coh}$ and a maximum amplitude of π rad onto the beam. To determine the random phase mask, we generate a 600 × 800 matrix of uniformly distributed random numbers between 0 and 1, and apply to this salt-and-pepper noise matrix a Gaussian filter of width $1/L_{\rm coh}$ defined below [28], which acts as a blur

$$G(k_x, k_y) = \frac{L_{\rm coh}^2}{2\pi} \exp\left(-\frac{k_x^2 + k_y^2}{2} L_{\rm coh}^2\right). \quad (1)$$

We then multiply the matrix by π so that the maximum phase amplitude of the added phase noise is π rad. Limiting the maximum phase amplitude to π rad ensures, as we show later, that the caustics formed after purely linear propagation through the cell are weak enough to not yield long-tailed intensity statistics [6]. The lenses L1 and L2 form a telescope that relays the active area of SLM2 to the entrance facet of the rubidium cell to form a fully resolved image of the phase mask realized on SLM2. The waveplates before the cell convert the polarization of the beam to left-handed circular to match the handedness of the σ_+ atomic transition. The lens L3 images the output facet of the cell onto the image plane of the camera, which records the intensity at the cell output.

Figures 1(b)–1(e) show the recorded output intensity distributions after linear propagation through the cell for representative phase masks with $L_{\rm coh}/D_0$ of 0.135, 0.075, 0.045, and 0.015, respectively. For all linear measurements, we increase the value of detuning from 600 MHz to 65.04 GHz and fix input beam power $P_{\rm in}$ to 4 mW. As shown in Figs. 1(b)–1(e), the added phase noise leads to redistribution of the beam intensity upon linear propagation, but is weak enough that no sharp caustics are formed. As we decrease the $L_{\rm coh}/D_0$ of noise (left to right), more "hotspots" are formed in the beam such that the intensity corresponding to the smallest $L_{\rm coh}/D_0$ [Fig. 1(e)] becomes more granular. Figures 1(f)–1(i) show the recorded intensities for the same phase masks as in the top panels (b)–(e), but with the nonlinearity turned on by changing the detuning to 600 MHz, and the beam power $P_{\rm in}$ to 90 mW. The nonlinearity sharpens the hotspots formed during linear propagation while preserving their underlying structure [6].

To quantify the intensity statistics, we record output intensity patterns for an ensemble of 500 random phase masks with the same $L_{\rm coh}$. We acquire these intensity datasets for nonlinear propagation through the cell at various incident beam powers $P_{\rm in}$ (30, 60, 90, and 115 mW) and various $L_{\rm coh}$ values (varied from 50 to 450 μm). We also record datasets for linear propagation through the cell. We only select the pixels in the acquired images that overlap with the beam to calculate the histogram of intensities in each dataset. These intensity histograms $N_H(I_N)$ are well described by a Weibull

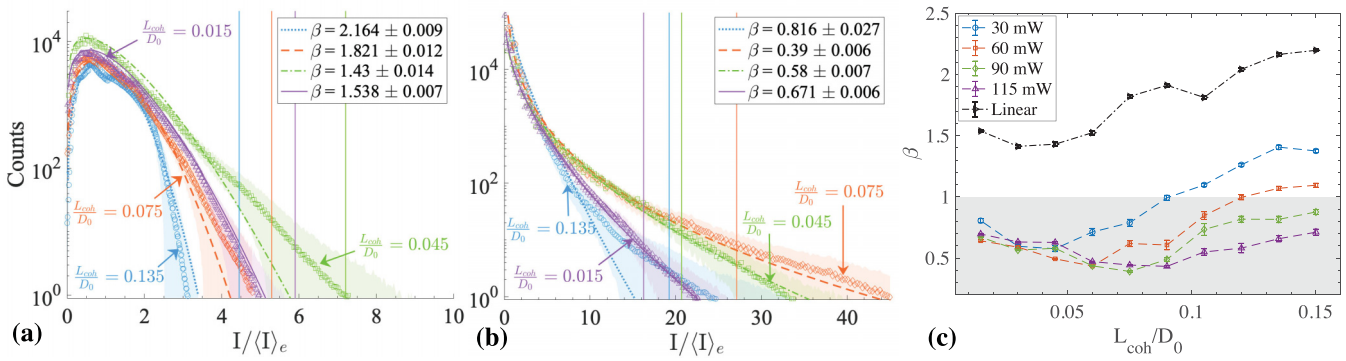

FIG. 2. (a) Measured intensity histograms (markers) and their respective Weibull distribution fits (lines) after (a) linear and (b) nonlinear propagation through the rubidium cell for L_{coh}/D_0 of 0.135 (blue, solid), 0.075 (red, dot-dashed), 0.045 (green, dashed), and 0.015 (purple, dotted). The value of P_{in} for the nonlinear datasets is 90 mW. The shaded regions around the respective plot markers represent the uncertainty of counts in the corresponding bins. The value of the parameter β for each fit is stated in the legend along with the corresponding uncertainty obtained through Monte Carlo simulations. The rogue-wave threshold intensities I_{RW} for each distribution are shown as solid vertical lines of the same color in both (a) and (b). (c) The variation of β with L_{coh}/D_0 for linear measurements (black triangles), and nonlinear measurements with P_{in} of 30 (blue circles), 60 (red squares), 90 (green diamonds), and 115 mW (purple triangles). The gray shaded region indicates the range of β corresponding to long-tailed intensity statistics.

distribution defined as follows [29]:

$$N_H(I_N) = N_{\text{total}} \frac{\beta}{\alpha} \left(\frac{I_N}{\alpha}\right)^{\beta-1} \exp\left[-\left(\frac{I_N}{\alpha}\right)^{\beta}\right], \qquad (2)$$

where $I_N = I/\langle I\rangle_e$ is the beam intensity normalized to the ensemble average of intensities in the entire dataset $\langle I\rangle_e$, N_{total} is the total number of counts in the dataset, and the parameters α and β are the scale and shape parameters of the distribution, respectively. Fully developed speckle patterns have an exponential distribution of intensities [16] and correspond to the scenario when $\beta = 1$. Long-tailed statistics have values of β smaller than 1 with caustic formation and rogue-wave behavior becoming more likely with smaller values of β. We estimate β for our measured intensity histograms by performing maximum likelihood estimation (MLE) fits to the Weibull distribution followed by Monte Carlo simulations to obtain the uncertainties of the fit parameters.

Figures 2(a) and 2(b) show the measured intensity statistics along with their respective Weibull distribution fits for linear and nonlinear propagation through the rubidium cell, respectively, for L_{coh}/D_0 of 0.135 (blue circles and dotted line), 0.075 (red diamonds and dashed line), 0.045 (green squares and dot-dashed line), and 0.015 (purple triangles and solid line). The input beam power P_{in} for the nonlinear datasets in Fig. 2(b) is 90 mW. The values of β estimated from the fits to each dataset are indicated in the legend. The nonlinear datasets in Fig. 2(b) show long-tailed statistics throughout, which is also manifested in the smaller estimated values of β for all L_{coh}/D_0 compared to the linear datasets in Fig. 2(a). The "tailiness" of the statistics can also be quantified in terms of the percentage of all counts in the histogram that exceed the rogue-wave threshold I_{RW}, which is defined as twice the average intensity in the highest third of events (or pixels with the highest third of recorded intensities) [10,30]. See Appendix A for details on the calculation of I_{RW} and the percentage of counts that exceed I_{RW}. For the linear results in Fig. 2(a), we do not observe any rogue events for L_{coh}/D_0 of 0.135 and 0.015, and only 0.001% and 0.005% for L_{coh}/D_0 of 0.075 and 0.045, respectively. In contrast, for the nonlinear results in Fig. 2(b), approximately 0.03%, 0.068%, 0.088%, and 0.058% of counts exceed I_{RW} for L_{coh}/D_0 of 0.135, 0.075, 0.045, and 0.015, respectively. Additionally, the values of I_{RW} for the nonlinear datasets are significantly larger than the linear dataset throughout (see Table I in Appendix A for the estimated values of I_{RW} and the rogue-wave percentages for all of the measured datasets). We also note that phase noise of smaller L_{coh}/D_0 has a wider angular spectral bandwidth (see Fig. 6 in Appendix C). This broadband noise seed should cause further broadening of the angular spectrum of the beam through four-wave mixing and lead to sharper caustics and longer-tailed intensity statistics. However, we do not observe a monotonic increase in the "tailiness" of intensity statistics as L_{coh}/D_0 is reduced in Fig. 2(b), which is also reflected in the associated values of β given in the legend. Instead, β is minimized for L_{coh}/D_0 of 0.075, and its distribution is the most long tailed.

Figure 2(c) shows the variation of β with L_{coh}/D_0 for linear measurements (black triangles) and nonlinear measurements with P_{in} of 30 (blue circles), 60 (red squares), 90 (green diamonds), and 115 mW (purple triangles). The shaded gray region represents the region where $\beta < 1$ and rogue-wave behavior is likely. As also shown in Fig. 2(a), $\beta > 1$ for purely linear propagation for all values of L_{coh}/D_0 considered here and we do not observe either rogue-wave behavior or the formation of a fully developed speckle pattern. The reasons for this result are: (i) the propagation distance (length of the cell) is short enough to be in the Fresnel region of the incident beam. Consequently, the number of scattering centers on the phase mask contributing to the field at any point on the observation plane is small enough for the central limit theorem to not be valid in a random walk statistical model of the field, which leads to non-Gaussian field statistics [31]. This argument is especially true for larger values of L_{coh}/D_0 for which there are fewer scattering centers for the input beam. (ii) The maximum phase amplitude of the added phase noise

is π, and hence small enough to not lead to strong focusing into sharp caustics after propagation through the cell [6]. The value of β for nonlinear measurements is smaller than β for linear measurements for all L_{coh}/D_0, which is consistent with the aforementioned increase in sharpness of caustics due to nonlinearity. The noteworthy feature, however, is that for nonlinear measurements, β is significantly more sensitive to the beam power P_{in} when L_{coh}/D_0 is larger than 0.075 than it is for smaller L_{coh}/D_0. This diminished sensitivity of the broadening of angular spectrum of the beam to nonlinearity when seeded by broadband phase noise shares similarities with the reduced effect of nonlinearity on the broadening of the modulational instability spectrum in an optical fiber for a low amplitude partially coherent broadband seed [32]. We further explore this observed phenomenon through numerical simulations.

III. NUMERICAL MODELING

The propagation of a field $\boldsymbol{E}(\boldsymbol{r},t) = E(x,y)e^{i(kz-\omega t)}\hat{\boldsymbol{e}}_L +$ c.c. through a spatially extended nonlinear medium, such as our rubidium cell, can be described by the $(2+1)$-D nonlinear Schrödinger equation (NLSE) [24] given below

$$\frac{\partial E}{\partial z} - \frac{i}{2k}\nabla_\perp^2 E = \frac{ik}{2\epsilon_0}P, \tag{3}$$

where $E(x,y)$ is the field envelope, ω is the angular frequency of the laser, k is the wave number, $\nabla_\perp^2 = \partial^2/\partial x^2 + \partial^2/\partial y^2$ is the transverse Laplacian, $P = \epsilon_0\chi(E)E$ is the atomic polarization, and $\chi(E)$ is the total atomic susceptibility that includes the linear as well as all orders of nonlinear response [24]. In our calculation of total susceptibility, we include the contributions from all the D2 transitions of rubidium. See Appendix B for more details. We use the split-step Fourier method [33] to solve Eq. (3), and obtain the field at any location (x,y,z) within the rubidium cell. We use Fresnel propagation for all linear propagation calculations [34]. For all simulations, we assume a transverse resolution of 2048×2048 pixels, a pixel size of 4.89 μm, and a longitudinal step size of 0.5 mm. We account for the slight longitudinal misalignment in our experimental setup by assuming that the beam waist is located 6 mm before the cell and add 1 cm of linear propagation after the cell.

Figures 3(a)–3(d) show the simulated output intensities for the same set of phase masks used in the experiment that were used for the measured output intensities shown in Figs. 1(f)–1(i). We also include an amplitude mask on the Gaussian beam to match the intensity of the Gaussian beam in our experiment [see Fig. 7(a)]. The simulated intensities in Figs. 3(a)–3(d), and the measured intensities in Figs. 1(f)–1(i) have very similar underlying intensity structures and sharpness of caustic features. Figure 3(e) shows the simulated intensity statistics for P_{in} of 90 mW, and L_{coh}/D_0 of 0.135 (blue circles), 0.075 (red diamonds), 0.045 (green squares), and 0.015 (purple triangles). We use 200 realizations of random phase masks of a particular L_{coh}/D_0 to calculate these intensity statistics. The simulated statistics show a good qualitative agreement with the measured statistics shown in Fig. 2(b) for the same set of parameters, and in both scenarios, the histogram corresponding to L_{coh}/D_0 of 0.075 is the most long tailed. We emphasize

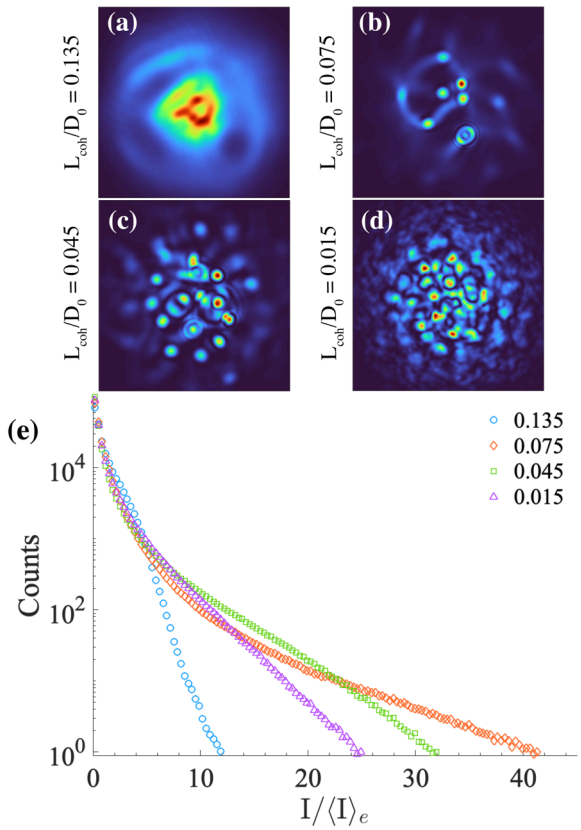

FIG. 3. (a) Simulated caustic patterns at the output of the cell for P_{in} of 90 mW, and L_{coh}/D_0 of (a) 0.135, (b) 0.075, (c) 0.045, and (d) 0.015. The phase masks used for these calculations were the same as the ones used in the experiment to capture the caustic patterns shown in Figs. 1(b)–1(e). (e) Simulated intensity statistics for P_{in} of 90 mW, and L_{coh}/D_0 of 0.135 (blue circles), 0.075 (red diamonds), 0.045 (green squares), and 0.015 (purple triangles).

that we do not expect a complete agreement between our measurements and numerical simulations due to several contributing factors, such as nonlocality in the nonlinear response of rubidium vapor [35], temperature variation within the cell leading to a spatial variation in the nonlinear susceptibility, aberrations in the imaging optics and the windows of the cell, and the pixel size of SLMs. Furthermore, the reinforcing nature of the self-focusing nonlinearity implies that our system is highly sensitive to any noise present in the experiment, which is difficult to account for in our simplified numerical model completely. However, the good qualitative agreement between our measurements and simulations allows us to study and draw reasonable conclusions about the propagation dynamics of the beam within the cell.

IV. DISCUSSION

To understand the interplay between phase noise induced distortion of the beam and the self-focusing nonlinearity, we use our simplified numerical model to study the propagation dynamics over a distance of 15 cm in the presence and in the absence of nonlinearity. Our use of the numerical model to understand the propagation dynamics is motivated by the fact that we cannot experimentally image the beam inside

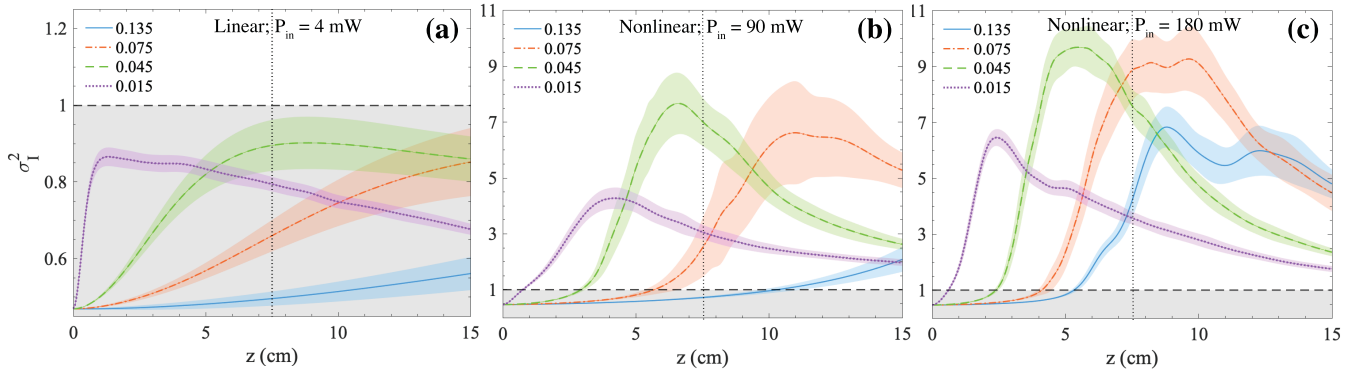

FIG. 4. The evolution of the scintillation index σ_I^2 with propagation distance z as predicted by our numerical model under (a) linear, and under [(b) and (c)] nonlinear propagation with P_{in} of 90 and 180 mW, respectively. The legend shows the values of L_{coh}/D_0 of the random phase mask added to the beam. The dashed black line indicates the threshold above which long-tailed intensity statistics start to emerge.

the nonlinear medium. We use the scintillation index σ_I^2 as a metric for the sharpness of caustics and monitor its variation with propagation distance z. The quantity σ_I^2 is the normalized variance of intensity defined as [36,37]

$$\sigma_I^2 = \frac{\langle I^2 \rangle - \langle I \rangle^2}{\langle I \rangle^2}. \tag{4}$$

Here, $\langle \cdots \rangle$ denotes the transverse spatial average over the entire field. Fully developed speckle patterns have a σ_I^2 of unity, while caustics with large intensity fluctuations in the transverse plane have σ_I^2 larger than unity. Also referred in the literature as the intensity "contrast" [12,31], the scintillation index has been used as a metric to identify the onset of branched flow—another instance of caustic formation due to the focusing of waves propagating through media with correlated disorder [37,38], and to characterize irradiance fluctuations in waves propagating through turbulence [12,36,39]. Figure 4(a) shows the evolution of σ_I^2 for a noisy Gaussian beam with L_{coh}/D_0 of 0.135 (blue, solid), 0.075 (red, dot-dashed), 0.045 (green, dashed), and 0.015 (purple, dotted) during linear propagation. The black horizontal dashed line indicates the threshold value of σ_I^2 above which sharp caustics characterized by larger fluctuations in intensity than a Gaussian speckle are observed. For a specific set of input parameters (P_{in} and L_{coh}), we average σ_I^2 at each z over 100 different phase masks. This averaged σ_I^2 is represented by the lines, and the shaded regions around the lines represent its standard deviation. Figures 4(b) and 4(c) show the evolution of σ_I^2 with z for nonlinear propagation with P_{in} of 90 and 180 mW, respectively, and the same set of values of L_{coh}/D_0 as in Fig. 4(a).

We note that in all of the scenarios shown in Figs. 4(a)–4(c), σ_I^2 at first increases with z, and then peaks as the phase noise on the beam morphs into intensity distortion. This rate of increase in σ_I^2 depends strongly on the grain size of the phase noise, as well as the nonlinearity. As also discussed previously in Refs. [12,31], we observe in Fig. 4(a) that σ_I^2 initially increases with z until it reaches a maximum when the various "facets" or grains of the added phase noise on the beam initially come to a focus along the minima of their gradients to form hotspots. When the grain size of the noise is much smaller than the beam diameter (such as when $L_{\text{coh}}/D_0 = 0.015$), the phase variations occur over a smaller area within the beam and so the phase gradients are larger and more densely packed [see Fig. 7(b)]. For purely linear propagation, these hotspots then diverge, thereby causing σ_I^2 to decrease with z. As the grain size of phase noise becomes larger, the phase gradients decrease in magnitude and become less densely packed [see Fig. 7(c)], which leads to fewer grains within the beam that focus into hotspots at larger z.

In the presence of nonlinearity, the hotspots formed after the initial reorganization of the beam continue to self-focus. Hence, σ_I^2 increases beyond unity and maximizes when at least one of the hotspots reaches a full width at half maximum (FWHM) size Δr of 25 ± 2.5 μm. A Gaussian beam of this FWHM size and an average power of 1.4 mW (say, P_{cr}) forms a self-trapped filament that propagates for at least 1.3 cm in the rubidium vapor without any change in its width before diverging due to absorption and diffraction. Filaments of the same width but smaller power than P_{cr} diverge more quickly, while those with power larger than P_{cr} undergo multiple self-focusing and defocusing cycles depending on their power [40]. For P_{in} of 90 mW and L_{coh}/D_0 of 0.015, more than two filaments of size Δr are formed when σ_I^2 is maximized such that the power in each filament is smaller than 0.9 mW [see Fig. 7(f)]. In contrast, for P_{in} of 90 mW, and $L_{\text{coh}}/D_0 \geqslant 0.045$, a single filament of size Δr with average power larger than 1 mW is formed when σ_I^2 is maximized [see Fig. 7(k)]. As shown in Fig. 4(b), this sharper intensity contrast between the "rogue" filaments and the background intensity in the beam for $L_{\text{coh}}/D_0 \geqslant 0.045$ results in a higher peak of σ_I^2 for these cases than when $L_{\text{coh}}/D_0 \leqslant 0.045$. When P_{in} is increased to 180 mW, the caustics become even sharper, and more filaments of size Δr are formed when σ_I^2 is maximized, which, as shown in Fig. 4(c), occurs at even smaller z for all cases. For L_{coh}/D_0 of 0.015 ($\geqslant$0.045), the average power in each filament is smaller (larger) than 1.4 mW (see Fig. 8). Hence, for noisy beams with $L_{\text{coh}}/D_0 \geqslant 0.045$, the propagation after the initial peak of σ_I^2 is followed by another cycle of self-focusing of filaments and subsequently, by diffraction. Nevertheless, even at such large beam powers, the small-grained phase noise seeds the formation of several filaments each containing less than P_{cr} power. This phenomenon limits the maximum intensity in a rogue feature and the tailiness of the intensity statistics. Finally, we note that σ_I^2 for $L_{\text{coh}}/D_0 < 0.045$

TABLE I. Table of the rogue-wave intensity threshold I_{RW} and the percentage of rogue waves observed RWP for measured intensity statistics at various input beam powers P_{in} and coherence lengths of the added phase noise to the beam L_{coh}/D_0.

P_{in} (mW)	L_{coh}/D_0	I_{RW}	RWP (%)
Linear	0.15	4.35	0
	0.135	4.46	0
	0.12	4.72	0
	0.105	4.8	0
	0.09	5.07	0
	0.075	5.29	0.001
	0.06	6.6	0.002
	0.045	7.2	0.005
	0.03	7.14	0.002
	0.015	5.9	0
30	0.15	6.46	0.007
	0.135	6.71	0.011
	0.12	6.82	0.012
	0.105	8.09	0.027
	0.09	10.12	0.046
	0.075	15.3	0.057
	0.06	16.26	0.123
	0.045	16.77	0.124
	0.03	15.63	0.097
	0.015	11.44	0.081
60	0.15	9.18	0.022
	0.135	9.73	0.019
	0.12	10.67	0.025
	0.105	16.44	0.046
	0.09	21.42	0.063
	0.075	21.85	0.125
	0.06	24.17	0.079
	0.045	24.57	0.049
	0.03	19.59	0.041
	0.015	14.83	0.075
90	0.15	13.67	0.036
	0.135	19.25	0.03
	0.12	19.92	0.04
	0.105	23.45	0.062
	0.09	24.39	0.056
	0.075	27.12	0.068
	0.06	26.31	0.068
	0.045	20.69	0.088
	0.03	20.09	0.033
	0.015	16.27	0.058
115	0.15	16.32	0.08
	0.135	17.77	0.083
	0.12	19.35	0.088
	0.105	19.14	0.095
	0.09	25.35	0.058
	0.075	26.06	0.061
	0.06	25.69	0.046
	0.045	21.37	0.049
	0.03	18.49	0.035
	0.015	14.84	0.091

($L_{coh}/D_0 \geqslant 0.045$) has little (large) variation between P_{in} of 90 and 180 mW at $z = 7.5$ Cm, or the length of the cell [dotted vertical line in Figs. 4(b) and 4(c)]. This result is a consequence of the initial beam reorganization followed by self-focusing cycle(s) occurring at shorter z as the phase noise becomes more granular, and is consistent with the diminished sensitivity of the likelihood of rogue-wave formation to nonlinearity observed experimentally.

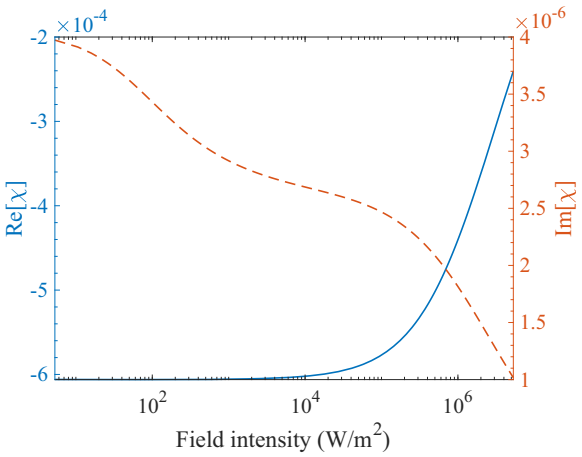

FIG. 5. Real (blue, left axis) and imaginary (red, right axis) parts of the total susceptibility of rubidium vapor versus the optical field intensity.

V. CONCLUSION

In summary, we have shown that the grain size of phase noise on a laser beam can be used to control rogue-wave formation in media with a self-focusing nonlinearity. The likelihood of rogue-wave formation is minimally affected by nonlinearity when the coherence length of phase noise is much smaller than the beam diameter. Our numerical simulations show that small-grained phase noise causes the beam power to be redistributed into multiple filaments rather than a single filament, which is formed when the phase noise has a longer correlation length. This redistribution of beam power into several filaments of smaller intensity limits the maximum intensity in rogue features relative to the background. Understanding the role of nonlinearity in amplifying the phase noise-induced intensity fluctuations on a field could be helpful in devising efficient mechanisms to mitigate these fluctuations for intense structured light propagating through a turbulent medium [41,42], and developing efficient radiance limiters using saturable nonlinear media [43].

ACKNOWLEDGMENTS

This work was supported by the US Office of Naval Research under Awards No. N00014-19-1-2247 and No. MURI N00014-20-2558. The authors would like to thank J.W. Kuper and G. Marcucci for helpful discussions.

APPENDIX A: ROGUE-WAVE THRESHOLDS AND LIKELIHOODS

As per the convention in optics [10], where we can only measure the intensity of events, the rogue-wave threshold $I_{RW}(=2I_S)$ here is defined in terms of the intensity as twice the mean intensity in the highest third of events I_S. Following the

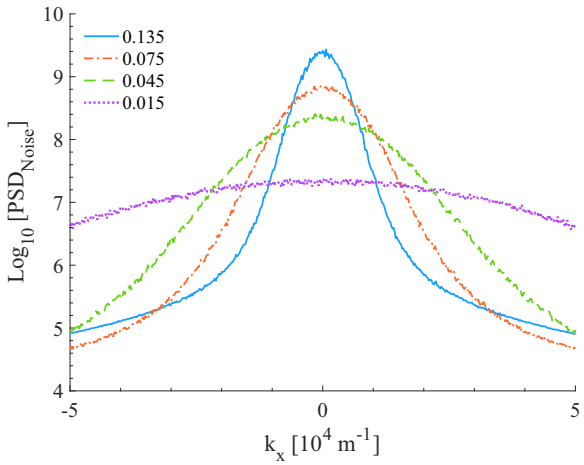

FIG. 6. The angular power spectral density (PSD) of phase noise $e^{i\phi_{\text{rand}}(x,y)}$ of various spatial coherence lengths L_{coh}. The legend states the values of the corresponding L_{coh} normalized to the beam diameter D_0.

method described in Ref. [30] for the calculation of I_{RW}, we first normalize the ensemble of recorded beam intensities on the camera for each dataset to the average intensity $\langle I \rangle_e$. Prior to normalization, we also crop the acquired images around the region of interest to discard the pixels that do not overlap with the beam. The local maxima of normalized intensities then yield the highest (or most intense) events (or pixels) in the ensemble, and I_S is given by the mean intensity of the highest third of these events. The rogue-wave percentage RWP is the percentage of pixels in the dataset with normalized intensities larger than I_{RW} with respect to the total number of pixels with nonzero intensities in the entire dataset. The estimated values of I_{RW} and RWP for the entire experimental dataset corresponding to Fig. 2(c) is shown in Table I below.

APPENDIX B: SUSCEPTIBILITY OF RUBIDIUM VAPOR

We use the method described in Ref. [44] to calculate the total susceptibility of rubidium vapor heated to 115 °C, and optically pumped at a detuning of 600 MHz above the ^{87}Rb D_2 $F = 1 \rightarrow F' = 2$ transition frequency. We first calculate the susceptibility contribution of each D_2 transition of rubidium to the total susceptibility using the equation (6.3.28) in Ref. [24], and the parameters in Ref. [45]. We include Doppler broadening of the spectrum of each resonant transition by convolving the respective spectrum with the Maxwell distribution of atom velocities [46]. We then sum these susceptibility contributions weighted by their oscillator strengths [47]. Figure 5 shows the real (blue, solid) and imaginary (red, dashed) parts of the total susceptibility χ of rubidium versus the optical pump intensity.

APPENDIX C: POWER SPECTRAL DENSITY OF THE PHASE NOISE

To calculate our phase masks $e^{i\phi_{\text{rand}}(x,y)}$, we first generate a matrix of uniformly distributed random numbers between 0 and 1. We then convolve the matrix with a Gaussian filter, whose response $G(k_x, k_y)$ in the angular frequency space (k_x, k_y) is given by Eq. (1) in the main text. We then multiply the entire matrix by π to rescale the phase variation to be between 0 and π rad. The spectral bandwidth of the phase noise can be estimated from its angular power spectral

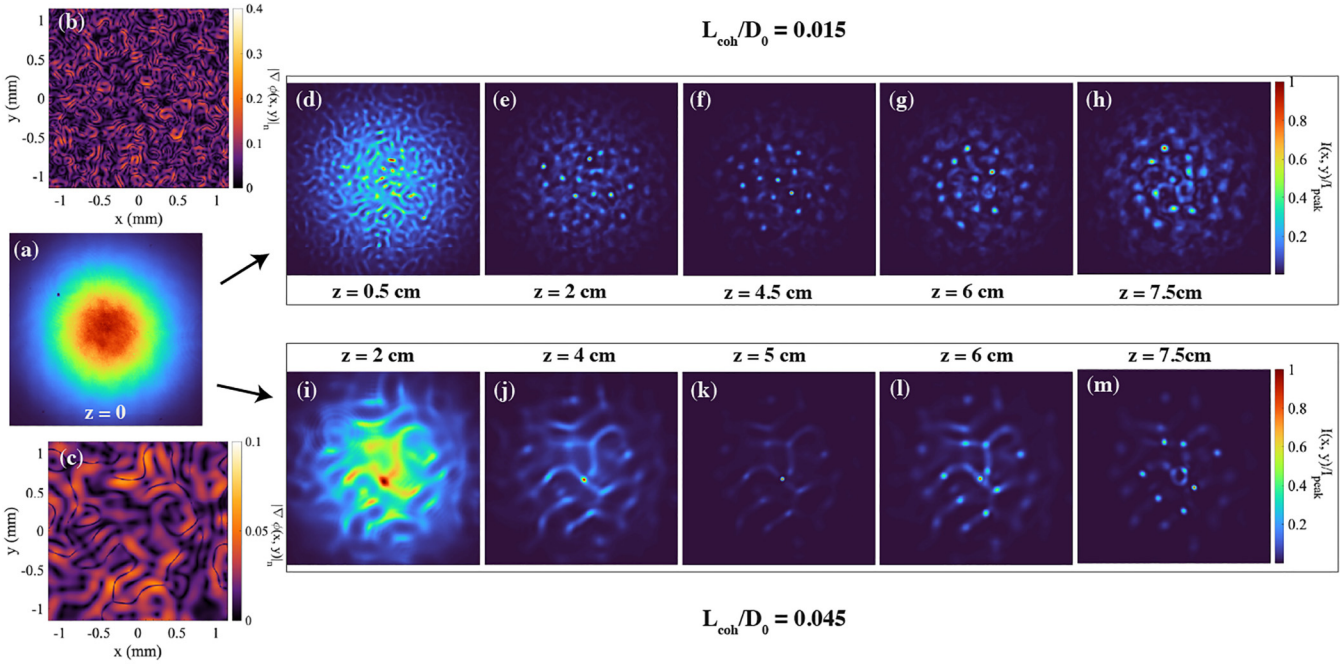

FIG. 7. (a) Input Gaussian beam intensity. Phase gradient map $|\nabla\phi(x, y)|$ for a sample mask with L_{coh}/D_0 of (b) 0.015 and (c) 0.045. The top panels (d)–(h) show the beam intensity at various propagation distances z within the cell for the phase gradient map shown in (b), and the bottom panels (i)–(m) show the beam intensity at various z for the phase gradient map shown in (c). The beam power P_{in} is 90 mW throughout. The intensity distributions in all panels are normalized with respect to the maximum intensity in the respective frames.

density (PSD), which we define as the squared magnitude of the 2D Fourier transform of $e^{i\phi_{\text{rand}}(x,y)}$. We take an ensemble average of the PSDs for 250 realizations of phase noise of a particular coherence length L_{coh}. In Fig. 6, we show the PSD of phase noise of normalized spatial coherence lengths L_{coh}/D_0 of 0.135 (blue, solid), 0.075 (red, dot-dashed), 0.045 (green, dashed) and 0.015 (purple, dotted), with D_0 being the Gaussian beam diameter. We note that the PSD of noise becomes more broadband as L_{coh}/D_0 is reduced, while the total noise power remains constant.

APPENDIX D: FIELD EVOLUTION THROUGH THE CELL

Figure 7(a) shows the intensity of the input Gaussian beam generated in our setup. As stated in the main text, the input field intensity in these numerical simulations is taken to be the same as the one generated in the experiment. Figures 7(b) and 7(c) show the phase gradient maps $|\nabla\phi(x, y)|$ of a representative random phase mask of coherence lengths L_{coh}/D_0 of 0.015 and 0.045, respectively. The top panels (d)–(h) show the normalized intensities of the beam at various propagation distances z stated in the panel label for the phase gradient map shown in Fig. 7(b). Similarly, the bottom panels (i)–(m) show the normalized intensities of the beam at various z for the phase gradient map shown in Fig. 7(c).

As shown in Figs. 7(d) and 7(i), the beam at first reorganizes by focusing along the minima of the respective phase gradient maps. This initial reorganization occurs at smaller z for phase noise of smaller grain size. The intensity hotspots on this reorganized beam then continue to self focus until at least one of the hotspots reaches the filament width Δr as shown in Figs. 7(f) and 7(k). The scintillation index of the beam σ_I^2 is maximized in this plane. The collapse of the filament is limited by absorption, saturation of the nonlinearity, and nonparaxiality [40]. For L_{coh}/D_0 of 0.015, multiple filaments of width Δr are formed at $z = 4.5$ Cm, and each filament has power smaller than P_{cr} required for forming a self-trapped filament that can propagate for several cm. Hence, these filaments diffract within a few mm as the other hotspots also self-focus and subsequently diffract. Around $z = 6$ Cm, absorption losses reduce the effect of nonlinearity, and the filaments start to diverge and σ_I^2 of the beam starts to decrease with z. For

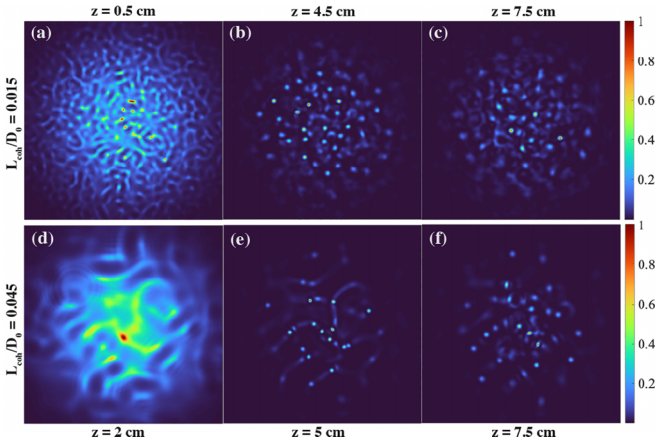

FIG. 8. The top panels (a)–(c) show the beam intensity at various propagation distances z within the cell for the phase gradient map shown in Fig. 7(b), and the bottom panels (d)–(f) show the beam intensity at various z for the phase gradient map shown in Fig. 7(c). The beam power P_{in} is 180 mW throughout. The intensity distributions in all panels are normalized with respect to the maximum intensity in the respective frames.

L_{coh}/D_0 of 0.045, a single filament of width Δr and power of 1.1 mW is formed at $z = 5$ Cm where σ_I^2 is also maximized. The large intensity contrast between the filament, and the background intensity of the beam leads to a much larger peak value of σ_I^2 than the peak value for L_{coh}/D_0 of 0.015 even though the power in the filament is still smaller than P_{cr}.

Figures 8(a)–8(c) show the beam evolution through the cell for the same phase gradient map as shown in Fig. 7(b), but at a beam power P_{in} of 180 mW. Similarly, Figs. 8(d)–8(f) show the beam evolution for the phase gradient map as shown in Fig. 7(c), and at a beam power P_{in} of 180 mW. Comparing Fig. 7(d) with Fig. 8(a), and Fig. 7(e) with Fig. 8(d), we note that the initial beam reorganization stage involving focusing along the minima of the respective phase gradients remains similar despite the higher power. Comparing Fig. 7(f) with Fig. 8(b) and Fig. 7(k) with Fig. 8(e), we note that the larger beam power gets distributed into several more filaments along the same underlying caustic pattern.

[1] D. R. Solli, C. Ropers, P. Koonath, and B. Jalali, Optical rogue waves, Nature (London) **450**, 1054 (2007).
[2] C. Liu, R. E. C. Van Der Wel, N. Rotenberg, L. Kuipers, T. F. Krauss, A. Di Falco, and A. Fratalocchi, Triggering extreme events at the nanoscale in photonic seas, Nat. Phys. **11**, 358 (2015).
[3] A. Mathis, L. Froehly, S. Toenger, F. Dias, G. Genty, and J. M. Dudley, Caustics and rogue waves in an optical sea, Sci. Rep. **5**, 12822 (2015).
[4] D. Pierangeli, F. Di Mei, C. Conti, A. J. Agranat, and E. DelRe, Spatial rogue waves in photorefractive ferroelectrics, Phys. Rev. Lett. **115**, 093901 (2015).
[5] D. Pierangeli, G. Musarra, F. Di Mei, G. Di Domenico, A. J. Agranat, C. Conti, and E. DelRe, Enhancing optical extreme events through input wave disorder, Phys. Rev. A **94**, 063833 (2016).
[6] A. Safari, R. Fickler, M. J. Padgett, and R. W. Boyd, Generation of caustics and rogue waves from nonlinear instability, Phys. Rev. Lett. **119**, 203901 (2017).
[7] R. Höhmann, U. Kuhl, H.-J. Stöckmann, L. Kaplan, and E. J. Heller, Freak waves in the linear regime: A microwave study, Phys. Rev. Lett. **104**, 093901 (2010).
[8] H. Degueldre, J. J. Metzger, T. Geisel, and R. Fleischmann, Random focusing of tsunami waves, Nat. Phys. **12**, 259 (2016).
[9] M. Onorato, S. Residori, U. Bortolozzo, A. Montina, and F. T. Arecchi, Rogue waves and their generating mechanisms in different physical contexts, Phys. Rep. **528**, 47 (2013).
[10] J. M. Dudley, F. Dias, M. Erkintalo, and G. Genty, Instabilities, breathers and rogue waves in optics, Nat. Photonics **8**, 755 (2014).

[11] J. M. Dudley, G. Genty, A. Mussot, A. Chabchoub, and F. Dias, Rogue waves and analogies in optics and oceanography, Nat. Rev. Phys. **1**, 675 (2019).

[12] G. Parry, P. N. Pusey, E. Jakeman, and J. G. McWhirter, Focussing by a random phase screen, Opt. Commun. **22**, 195 (1977).

[13] M. S. Longuet-Higgins, The statistical analysis of a random, moving surface, Philos. T. R. Soc. A **249**, 321 (1957).

[14] C. Fochesato, S. Grilli, and F. Dias, Numerical modeling of extreme rogue waves generated by directional energy focusing, Wave motion **44**, 395 (2007).

[15] J. W. Goodman, Some fundamental properties of speckle, J. Opt. Soc. Am. **66**, 1145 (1976).

[16] J. W. Goodman, *Speckle Phenomena in Optics: Theory and Applications* (Roberts and Company Publishers, Englewood, Colorado, USA, 2007).

[17] Th. M. Nieuwenhuizen and M. C. W. Van Rossum, Intensity distributions of waves transmitted through a multiple scattering medium, Phys. Rev. Lett. **74**, 2674 (1995).

[18] F. T. Arecchi, U. Bortolozzo, A. Montina, and S. Residori, Granularity and inhomogeneity are the joint generators of optical rogue waves, Phys. Rev. Lett. **106**, 153901 (2011).

[19] Y. Bromberg and H. Cao, Generating non-Rayleigh speckles with tailored intensity statistics, Phys. Rev. Lett. **112**, 213904 (2014).

[20] P. Walczak, S. Randoux, and P. Suret, Optical rogue waves in integrable turbulence, Phys. Rev. Lett. **114**, 143903 (2015).

[21] M. Närhi, B. Wetzel, C. Billet, S. Toenger, T. Sylvestre, J.-M. Merolla, R. Morandotti, F. Dias, G. Genty, and J. M. Dudley, Real-time measurements of spontaneous breathers and rogue wave events in optical fibre modulation instability, Nat. Commun. **7**, 1 (2016).

[22] M. Onorato, A. R. Osborne, and M. Serio, Modulational instability in crossing sea states: A possible mechanism for the formation of freak waves, Phys. Rev. Lett. **96**, 014503 (2006).

[23] A. Montina, U. Bortolozzo, S. Residori, and F. T. Arecchi, Non-Gaussian statistics and extreme waves in a nonlinear optical cavity, Phys. Rev. Lett. **103**, 173901 (2009).

[24] R. W. Boyd, *Nonlinear optics*, 4th ed. (Academic press, San Diego, California, USA, 2020).

[25] S. Birkholz, E. T. J. Nibbering, C. Brée, S. Skupin, A. Demircan, G. Genty, and G. Steinmeyer, Spatiotemporal rogue events in optical multiple filamentation, Phys. Rev. Lett. **111**, 243903 (2013).

[26] A. N. Black, S. Choudhary, E. S. Arroyo-Rivera, H. Woodworth, and R. W. Boyd, Suppression of nonlinear optical rogue wave formation using polarization-structured beams, Phys. Rev. Lett. **129**, 133902 (2022).

[27] A. Zannotti, D. Ehrmanntraut, and C. Denz, Enhanced optical rogue waves by scattering caustic networks in tailored disorder, in *Nonlinear Optics* (Optical Society of America, 2019) pp. NW3B–2.

[28] T. Shirai, O. Korotkova, and E. Wolf, A method of generating electromagnetic Gaussian Schell-model beams, J. Opt. A Pure Appl. Op. **7**, 232 (2005).

[29] W. Weibull, A statistical distribution function of wide applicability, J. Appl. Mech. **18**, 293 (1951).

[30] D. Pierangeli, G. Perini, V. Palmieri, I. Grecco, G. Friggeri, M. De Spirito, M. Papi, E. DelRe, and C. Conti, Extreme transport of light in spheroids of tumor cells, Nat. Commun. **14**, 4662 (2023).

[31] E. Jakeman, Speckle statistics with a small number of scatterers, Optical Engineering **23**, 453 (1984).

[32] D. M. Nguyen, T. Godin, S. Toenger, Y. Combes, B. Wetzel, T. Sylvestre, J.-M. Merolla, L. Larger, G. Genty, F. Dias *et al.*, Incoherent resonant seeding of modulation instability in optical fiber, Opt. Lett. **38**, 5338 (2013).

[33] G. Agrawal, *Nonlinear Fiber Optics*, 5th ed. (Academic Press, Kidlington, UK, 2013).

[34] J. W. Goodman, *Introduction to Fourier optics*, 3rd ed. (Roberts & Co., Englewood, Colorado, USA, 2005).

[35] D. Suter and T. Blasberg, Stabilization of transverse solitary waves by a nonlocal response of the nonlinear medium, Phys. Rev. A **48**, 4583 (1993).

[36] L. C. Andrews, R. L. Phillips, C. Y. Hopen, and M. A. Al-Habash, Theory of optical scintillation, J. Opt. Soc. Am. A **16**, 1417 (1999).

[37] S. Barkhofen, J. J. Metzger, R. Fleischmann, U. Kuhl, and H.-J. Stöckmann, Experimental observation of a fundamental length scale of waves in random media, Phys. Rev. Lett. **111**, 183902 (2013).

[38] A. Patsyk, U. Sivan, M. Segev, and M. A. Bandres, Observation of branched flow of light, Nature (London) **583**, 60 (2020).

[39] G. Gbur, Partially coherent beam propagation in atmospheric turbulence [Invited], J. Opt. Soc. Am. A **31**, 2038 (2014).

[40] M. Feit and J. A. Fleck, Beam nonparaxiality, filament formation, and beam breakup in the self-focusing of optical beams, J. Opt. Soc. Am. B **5**, 633 (1988).

[41] M. A. Cox, N. Mphuthi, I. Nape, N. Mashaba, L. Cheng, and A. Forbes, Structured light in turbulence, IEEE J. Sel. Top. Quantum Electron. **27**, 1 (2020).

[42] R. J. Watkins, K. Dai, G. White, W. Li, J. K. Miller, K. S. Morgan, and E. G. Johnson, Experimental probing of turbulence using a continuous spectrum of asymmetric oam beams, Opt. Express **28**, 924 (2020).

[43] A. Schweinsberg, J. W. Kuper, and R. W. Boyd, Loss of spatial coherence and limiting of focal plane intensity by small-scale laser-beam filamentation, Phys. Rev. A **84**, 053837 (2011).

[44] A. Safari, Resonant light-matter interaction for enhanced control of exotic propagation of light, Ph.D. thesis, Université d'Ottawa/University of Ottawa, 2019.

[45] D. A. Steck, Rubidium 85 and 87 D line data, http://steck.us/alkalidata (2023).

[46] R. Loudon, *The Quantum Theory of Light*, 3rd ed. (OUP Oxford, Oxford, UK, 2000).

[47] P. Siddons, C. S. Adams, C. Ge, and I. G. Hughes, Absolute absorption on rubidium D lines: Comparison between theory and experiment, J. Phys. B: At., Mol. Opt. Phys. **41**, 155004 (2008).